



Article

Band Polarization Effect on the Kondo State in a Zigzag Silicene Nanoribbon

Ginetom S. Diniz ^{1,2} , Edson Vernek ² and George B. Martins ^{2,*} ¹ Curso de Física, Universidade Federal de Jataí, Jataí 75801-615, GO, Brazil; ginetom@gmail.com² Instituto de Física, Universidade Federal de Uberlândia, Uberlândia 38400-902, MG, Brazil; vernek@ufu.br

* Correspondence: gbmartins@ufu.br

Abstract: Using the Numerical Renormalization Group method, we study the properties of a quantum impurity coupled to a zigzag silicene nanoribbon (ZSNR) that is subjected to the action of a magnetic field applied in a generic direction. We propose a simulation of what a scanning tunneling microscope will see when investigating the Kondo peak of a magnetic impurity coupled to the metallic edge of this topologically non-trivial nanoribbon. This system is subjected to an external magnetic field that polarizes the host much more strongly than the impurity. Thus, we are indirectly analyzing the ZSNR polarization through the STM analysis of the fate of the Kondo state subjected to the influence of the polarized conduction electron band. Our numerical simulations demonstrate that the spin-orbit-coupling-generated band polarization anisotropy is strong enough to have a qualitative effect on the Kondo peak for magnetic fields applied along different directions, suggesting that this contrast could be experimentally detected.

Keywords: Kondo effect; topological insulators; silicene



Citation: Diniz, G.S.; Vernek, E.; Martins, G.B. Band Polarization Effect on the Kondo State in a Zigzag Silicene Nanoribbon. *Nanomaterials* **2022**, *12*, 1480. <https://doi.org/10.3390/nano12091480>

Academic Editors: Eugene Kogan and Béla Pécz

Received: 25 February 2022

Accepted: 18 April 2022

Published: 27 April 2022

Publisher's Note: MDPI stays neutral with regard to jurisdictional claims in published maps and institutional affiliations.



Copyright: © 2022 by the authors. Licensee MDPI, Basel, Switzerland. This article is an open access article distributed under the terms and conditions of the Creative Commons Attribution (CC BY) license (<https://creativecommons.org/licenses/by/4.0/>).

1. Introduction

Topological insulators have attracted much attention since the proposal by Charles Kane and Eugene Mele [1,2] was made, stating that the spin-orbit interaction in graphene could reproduce the properties of the seminal model proposed by Duncan Haldane in 1988 [3], which displayed topological properties similar to those of the quantum Hall effect; however, without a net magnetic field. The topological effect in the so-called Kane–Mele model, which was supposed to display ‘spin-momentum-locked’ edge states at the borders of a graphene finite-size sample, was dubbed the ‘Quantum Spin Hall Effect’. Unfortunately, graphene’s spin-orbit interaction (essential for the opening of a gap and the spin-momentum-locking effect) proved to be vanishingly small, and this non-trivial topological state had to be pursued in a specific quantum-well system, CdTe/HgTe [4,5]. However, it so happens that the so-called *Xenes* (silicene, germanene and stanene, among others), which form monolayers that share many similarities with graphene, have a spin-orbit interaction that is three orders of magnitude larger than graphene [6]. This happens because of an effect called ‘buckling’, where, contrary to graphene, the two sublattices forming the *Xenes*’ hexagonal structure are not coplanar, rather, they are shifted vertically. Thus, *Xenes* can be very closely described by the Kane–Mele model, and therefore a zigzag silicene nanoribbon (ZSNR), for example, will present a 1D helical state at its edges: counter-propagating spin-momentum-locked states that form what became known as a helical 1D liquid. Reviews of *Xenes* properties can be found in Refs. [7–15]. Investigations treating more specifically the topological properties of silicene, germanene, and stanene are found in Refs. [16,17]. A detailed description of how to obtain the Kane–Mele model as a low energy effective model for silicene, germanene, and stanene, starting from first principles calculations, can be found in Ref. [6].

Given that the helical edge state is protected by time-reversal symmetry [1,2], and is thus immune, in principle, to potential scattering, it is interesting to ask what the influence

is on the helical state of magnetic impurities that couple to it. Indeed, due to the helical state property of spin-momentum locking, back-scattering has to involve a spin-flip; thus, it cannot occur for pure potential scattering, while a magnetic impurity, which can flip its spin too, would provide a back-scattering mechanism. For example, the fact that the conductance of the helical state in CdTe/HgTe was measured to be $G < G_0 = 2e^2/h$ and decreased with lowering temperature, was attributed, at least initially [18,19], to the presence of either magnetic impurities coupled to the edges or to the presence of trapped electrons that interact with the helical state [20]. It should be noticed that, recently, an alternative interpretation to the conductance measurements in CdTe/HgTe quantum-wells have been proposed, see Refs. [18,19]. In both cases, this can be modeled by a single-impurity Anderson model (SIAM) [21], and points to the possible occurrence of a Kondo effect [22]. For a detailed discussion of the various mechanisms invoked to explain the $G < G_0$ anomalous conductance, see Ref. [23].

Few studies have directly addressed the Kondo effect for the case of a quantum magnetic impurity coupled to the edge state associated with the Kane–Mele model. First, Goth et al. [24] have used the continuous time quantum Monte Carlo method to study the spatial dependence of the single-particle spectral functions and spin–spin correlation functions when a single quantum impurity couples to the helical edge state. They concluded that, contrary to what happens for a one-dimensional conductor, in a helical liquid, magnetic impurities cannot block transport below the Kondo temperature. Rather, the current circumvents the impurity. A similar result was obtained by Allerdt et al. [25,26], using a recently developed numerical method combined with the Density Matrix Renormalization Group method [27,28]. It should also be noted that Weymann et al. [29], using the Numerical Renormalization Group (NRG) method, coupled to the Density Functional Theory, have conducted a detailed study of the Kondo effect of a cobalt impurity deposited on top of a 2D silicene sheet. As the host for their impurity has no edges, just bulk, they did not analyze any of the properties of the edge state in relation to Kondo coupling. However, they did perform a careful analysis of the effects of gating (variation of the band filling of the host), as well as the effect of an external magnetic field acting just on the cobalt impurity.

In the present work, using NRG, we intend to expand the research conducted on the Kondo effect stemming from a quantum impurity coupled to a ZSNR. We study the effect of a magnetic field applied upon the host, not just upon the impurity. It is known that the magnetic polarization of the bands, due to an external magnetic field, affects the Kondo state [30], mainly if the host displays spin-orbit interaction, as the band magnetic polarization becomes anisotropic. Since there is ample choice of what kind of magnetic impurity may be adsorbed into the ZSNR, demonstrating a wide variation in their g -factor, we will explicitly consider a situation where the host g -factor, denoted g_b (see Equation (2)), is considerably larger than the impurity g -factor, denoted g_{imp} (see Equation (3)). This is intended to showcase the effect on the Kondo state caused by the band magnetic polarization.

2. Theoretical Model

2.1. Model Hamiltonian

To model a magnetic impurity coupled to a ZSNR, as depicted in Figure 1, we use a SIAM-like Hamiltonian [21], given by

$$H = H_{\text{ZSNR}} + H_{\text{imp}} + H_{\text{tip}} + H_{\text{ZSNR-imp}} + H_{\text{imp-tip}}, \quad (1)$$

where the first term describes a ZSNR, subjected to an external magnetic field and modeled by a tight-binding Hamiltonian, which in real space reads as

$$H_{\text{ZSNR}} = \sum_{i\sigma} \epsilon_0 c_{i\sigma}^\dagger c_{i\sigma} - \left[t \sum_{\langle i,j \rangle \sigma} c_{i\sigma}^\dagger c_{j\sigma} - i \frac{\lambda_{\text{SO}}}{3\sqrt{3}} \sum_{\langle\langle i,j \rangle\rangle \sigma} \sigma v_{ij} c_{i\sigma}^\dagger c_{j\sigma} + \text{H.c.} \right] + \mu_B g_b \sum_i \vec{S}_i \cdot \vec{B}. \tag{2}$$

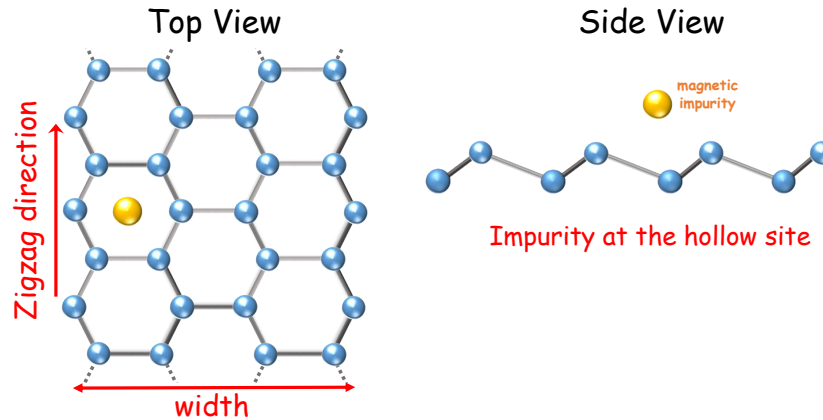


Figure 1. Schematic representation of a ZSNR (top view and side view) with a magnetic impurity located at the so-called hollow site.

The first term in Equation (2) is the on-site energy, where the operator $c_{i\sigma}^\dagger$ ($c_{i\sigma}$) creates (annihilates) an electron with energy ϵ_0 and spin σ in the i -th site of the ZSNR. The second term is the nearest-neighbor (NN) π -band tight-binding term, where $t_{ij} = t$ is the hopping between NN sites. The introduction of a next-NN hopping will not qualitatively alter the results, since the presence of the impurity in a hollow-site configuration already breaks particle-hole symmetry, see Ref. [31] for further details. The third term is the intrinsic next-NN spin-orbit coupling (SOC) λ_{SO} , where $v_{ij} = +1$ if the NNN hopping is anticlockwise and $v_{ij} = -1$ if it is clockwise (in relation to the positive z -axis) [6]. Note that, in the third term, $\sigma = \pm$ for subindex $\sigma = \uparrow, \downarrow$, respectively. The fourth term is the Zeeman interaction due to an external magnetic field $\vec{B} = (B_x, B_y, B_z)$, where μ_B stands for the Bohr magneton, g_b is the conduction electron g -factor for the ZSNR, and \vec{S}_i is the conduction electron spin density in site i . Finally, all calculations are conducted with the ZSNR at half-filling and we use the NN hopping t as our unit of energy. It is worth mentioning that the SOC term is equivalent to an effective magnetic field perpendicular to the ZSNR (z -direction). This is discussed in Appendix B.

The second term in Equation (1) describes the impurity, including a Zeeman interaction,

$$H_{\text{imp}} = \epsilon_d (n_{\text{imp},\uparrow} + n_{\text{imp},\downarrow}) + U n_{\text{imp},\uparrow} n_{\text{imp},\downarrow} + \mu_B g_{\text{imp}} \vec{S}_d \cdot \vec{B}, \tag{3}$$

where $n_{\text{imp},\sigma} = d_\sigma^\dagger d_\sigma$ and d_σ^\dagger (d_σ) creates (annihilates) an electron at the impurity with orbital energy ϵ_d , while double occupancy of the impurity costs Coulomb energy U . In the third (Zeeman) term, g_{imp} stands for the impurity g -factor and \vec{S}_d is the impurity spin operator.

As most experimental setups that are employed to probe such systems count with the aid of a scanning tunneling microscope (STM) device, we have also added a third term to Equation (1), referring to an STM tip, which is modeled by the Hamiltonian $H_{\text{tip}} = \sum_{M,k,\sigma} \epsilon_{Mk} c_{Mk\sigma}^\dagger c_{Mk\sigma}$, where $c_{Mk\sigma}^\dagger$ ($c_{Mk\sigma}$) creates (annihilates) an electron with momentum k and spin σ in the metallic STM tip. The fourth term of Equation (1), which couples the impurity to the ZSNR, is given by

$$H_{\text{ZSNR-imp}} = \sum_{j,\sigma} \left(V_{j\sigma} c_{j\sigma}^\dagger d_\sigma + \text{H.c.} \right), \tag{4}$$

while the fifth term, which couples the impurity to the STM tip, reads as

$$H_{\text{imp-tip}} = \sum_{k,\sigma} \left(V_k c_{k,\sigma}^\dagger d_\sigma + \text{H.c.} \right). \quad (5)$$

In Equation (4), $V_{j\sigma}$ represents the impurity-ZSNR hopping amplitude to the six neighboring silicon atoms when the impurity is in the hollow-site configuration (see Figure 1). Assuming the same coupling strength to the impurity for all the nearest-neighbor Si atoms, we will set $V_{j\sigma} \equiv V_0$. We have checked that considering the influence of the buckling in the values of $V_{j\sigma}$, i.e., having different hoppings from the impurity to different sublattice-sites, does not qualitatively change the results obtained. The value we used for the sublattice vertical shift was 0.46 \AA [17]. In addition, assuming a constant density of states at the tip, ρ_{tip} , and taking $V_k \equiv V_{\text{tip}}$ in Equation (5), we may write the tip hybridization function as $\Gamma_{\text{tip}} = \pi V_{\text{tip}}^2 \rho_{\text{tip}}$. Based on the results presented by Weymann et al. [29], the energetically most favorable position for a cobalt impurity in silicene is the so-called hollow-site configuration (depicted in Figure 1). We will thus present all our results for this impurity-coupling configuration. Finally, to keep the analysis simple, we will neglect the Rashba SOC, so that the only terms that control the band gap are the external magnetic field and the intrinsic SOC, λ_{SO} .

2.2. Tight-Binding Bands

The tight-binding ZSNR Hamiltonian (Equation (2)) can be diagonalized by a Fourier transform to reciprocal space, resulting in

$$H_{\text{ZSNR}} = \sum_k \Psi_k^\dagger \mathcal{H}_{\text{ZSNR}} \Psi_k, \quad (6)$$

where $\Psi_k^\dagger = (c_{k\uparrow}^\dagger, c_{k\downarrow}^\dagger)$, $c_{k\sigma}^\dagger$ creates an electron with wave vector k and spin $\sigma = \uparrow, \downarrow$, and the spectra is obtained by numerical diagonalization. In Figure 2, we show the resulting band structure (left panels) and total density of states (DOS, right panels) for a ZSNR with $N = 26$ zigzag chains. The top panels have results for the vanishing magnetic field, with $\lambda_{SO} = 0.0$ (black curve) and $\lambda_{SO} = 0.1$ (red curve). In Ref. [6], the λ_{SO} estimates for silicene, germanene, and stanene are (in meV), respectively, 3.9, 43.0, and 29.9. Thus, we are assuming a relatively high-value for λ_{SO} (more appropriate for germanene); nonetheless, the qualitative behavior of the results presented in the following sections still holds for the case of a lower λ_{SO} . In the absence of intrinsic SOC, the well-known dispersionless bands at the Fermi energy, associated to the edge states present in a graphene ZNR [32], can be observed in Figure 2a (black curve), with a noticeable peak in the respective DOS, Figure 2b. The introduction of the intrinsic SOC adds dispersion to these metallic bands (red curve), besides polarizing the edge state spins [17]. When a magnetic field is applied to the ZSNR, as shown in Figure 2c, there is a spin splitting proportional to the Zeeman energy. As a consequence, the dispersionless $\lambda_{SO} = 0.0$ energy bands at the Fermi level (black curve) are now symmetrically (particle-hole) shifted, but still present sharp singularities in the DOS, which are only suppressed for $\lambda_{SO} \neq 0$ (red curve), as shown in Figure 2d. In the next sections, we will demonstrate that these changes in the DOS have interesting consequences to the Kondo effect.

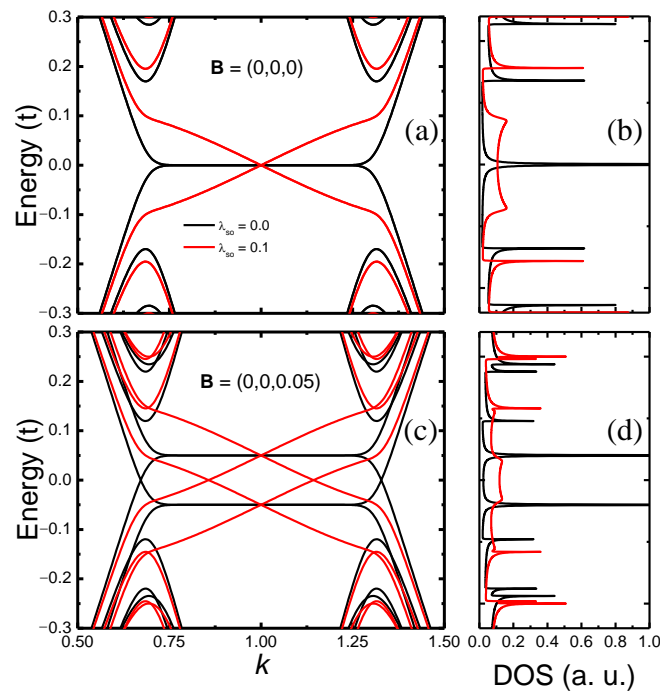


Figure 2. (a,c) $N = 26$ ZSNR energy bands, as a function of momentum, and the respective total DOS, panels (b,d), for energies close to the Fermi level. Panel (a) presents results in the absence of magnetic field for two different sets of parameters [see legend in panel (a)], while panel (c) presents results for the same parameters as in panel (a), but with a magnetic field along the z -direction. Labels for each curve in all panels are displayed in (a).

2.3. Hybridization Function

The impurity Green's function $\hat{G}_{\text{imp}}(k, \omega)$ can be written as

$$\hat{G}_{\text{imp}}(k, \omega) = \left[(\omega - \epsilon_d) \sigma_0 - \hat{\Sigma}^{(\text{int})}(k, \omega) - \hat{\Sigma}^{(0)}(k, \omega) \right]^{-1}, \quad (7)$$

where $\hat{\Sigma}^{(\text{int})}(k, \omega)$ is the interaction self-energy, while $\hat{\Sigma}^{(0)}(k, \omega) = \hat{V} \hat{G}_{\text{ZSNR}}(k, \omega) \hat{V}^\dagger$ is the hybridization self-energy, with $\hat{V} = V_0 \sigma_0$ and $\hat{G}_{\text{ZSNR}}(k, \omega) = [\omega \sigma_0 - \mathcal{H}_{\text{ZSNR}}]^{-1}$. For a magnetic field applied along an arbitrary direction, $\hat{\Sigma}^{(0)}(k, \omega)$ has finite off-diagonal terms and we have to deal with a spin-mixing hybridization function [33,34]

$$\hat{\Gamma}(\omega) = \frac{1}{2i} \int_{-\pi}^{\pi} \left[\hat{\Sigma}^{(0)}(k, \omega - i0^-) - \hat{\Sigma}^{(0)}(k, \omega + i0^+) \right] dk. \quad (8)$$

This positive-definite Hermitian matrix can be decomposed in terms of Pauli matrices as $\hat{\Gamma}(\omega) = \sum_{\alpha=0,x,y,z} d_\alpha(\omega) \sigma_\alpha$, where all $d_\alpha(\omega)$ are real quantities. In particular, $d_0(\omega)$ is proportional to the conduction-band density of states. More specifically, the spin-resolved density of states is given by $\rho_{\sigma\sigma}(\omega) = \Gamma_{\sigma\sigma}(\omega) / (\pi V^2)$. Thus, $\rho_{\uparrow\uparrow} \propto d_0 + d_z$, $\rho_{\downarrow\downarrow} \propto d_0 - d_z$, resulting in $\rho = \rho_{\uparrow\uparrow} + \rho_{\downarrow\downarrow} \propto 2d_0$.

In Figure 3, we show, in the main panels, the coefficients $d_\alpha(\omega)$ of the hybridization function decomposition, in terms of the Pauli matrices σ_α , for the vanishing SOC. Each panel contains a different magnetic field configuration: it vanishes in panel (a), and it takes values $B_\alpha = 0.001$, for $\alpha = x, y, z$ in panels (b) to (d), respectively. The coefficients d_α contain important physical information about the system under study. For instance, in panel (a), in the absence of any interaction (vanishing SOC and magnetic field), the system presents a localized edge state at the Fermi level, as shown in Figure 2b, whose signature is captured by the d_0 coefficient, which is directly proportional to the ZSNR DOS (see above), while all the other coefficients vanish. For the case of finite magnetic field [panels (b) to (d)] the d_0 peak observed in panel (a) is spin-split due to the Zeeman interaction. In addition,

for each field orientation B_α , besides d_0 , only the corresponding coefficient d_α will be finite, although its dependence with ω is the same for all three directions, as can be observed in Figure 3b–d. This is a consequence of SU(2) symmetry (spatial isotropy of the conduction electron spins) in the absence of SOC.

If the intrinsic SOC is turned on, i.e., $\lambda_{SO} = 0.1$, first, as implied from Figure 2b (red curve), the peak in d_0 at the Fermi energy should be strongly suppressed and broadened, as shown in the inset to Figure 3a. In addition, the spatial isotropy observed for the vanishing SOC is broken. Indeed, as shown in the Appendix B, the intrinsic SOC may be interpreted as a k -dependent effective magnetic field along the z -axis. Thus, the results for magnetic field along the x - or y -axis should be identical (with y interchanged for x , see the insets in Figure 3b,c), but they should differ from the results for the magnetic field along the z -axis (see inset in Figure 3d). It is also important to mention that even though the ZSNR preserves particle-hole (p - h) symmetry when SOC and magnetic fields are considered, for the impurity located at the hollow site, the system is non-bipartite; therefore, the hybridization function does not preserve particle-hole symmetry (p - h symmetry) [35]. However, the broken p - h symmetry is highly pronounced only for high energies (not shown in the figures).

Before presenting the NRG results, we wish to discuss the results for the ZSNR band polarization $\langle S_\alpha^b \rangle$, which is calculated as $\sum_k \langle k | S_\alpha^b | k \rangle$, where $|k\rangle$ are the eigenstates of \mathcal{H}_{ZSNR} in Equation (6). The sum is over the first Brillouin zone, up to the Fermi energy. Figure 4 shows the results for vanishing SOC (black curve), when all magnetic field orientations produce the same result, and for $\lambda_{SO} = 0.1$, where the $\langle S_{x/y}^b \rangle$ for a magnetic field applied along the x or y -axis are identical (see red and green curves), while the polarization $\langle S_z^b \rangle$ for a magnetic field applied along the z -axis is suppressed (blue curve). The anisotropy observed in Figure 4 was already discussed in connection with Figure 3, being caused by the SOC effective magnetic field oriented along the z -axis. As shown in the next section, the considerably smaller polarization at finite SOC for the z -axis when compared to the x - and y -axis, has sizable consequences for the Kondo effect when $g_{imp} = 0$, which would be experimentally detectable for a real situation where the magnetic impurity is such that $g_{imp} \ll g_b$ (this subject is discussed in detail in Appendix A).

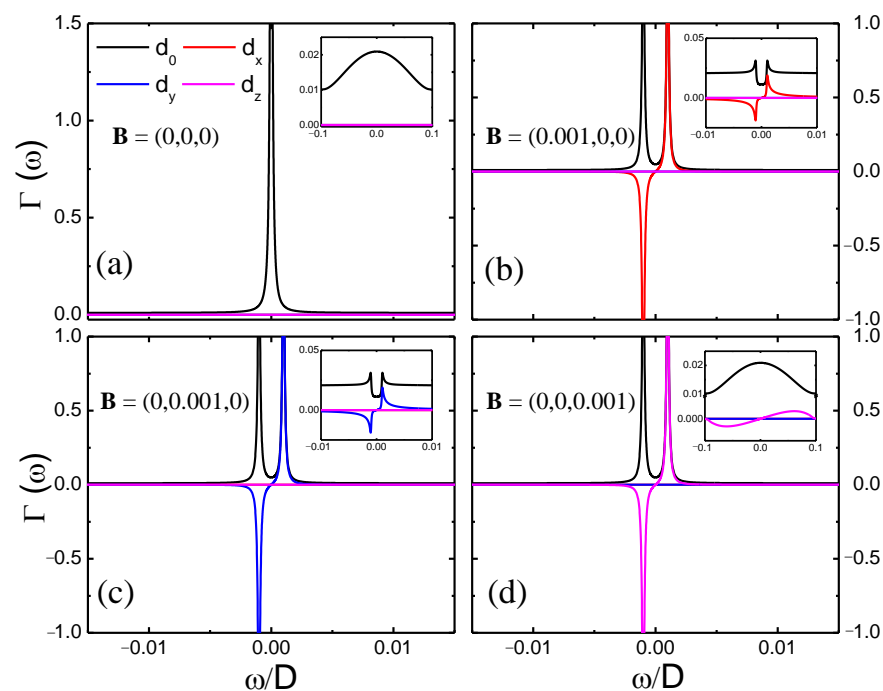


Figure 3. (a–d) Hybridization function coefficients $d_{\alpha=0,x,y,z}(\omega)$ for applied magnetic field along different directions, for an impurity placed at the hollow-site configuration (at the edge). The insets show the coefficients for $\lambda_{SO} = 0.1$. For all panels $N = 26$ and $V_0 = 0.05$.

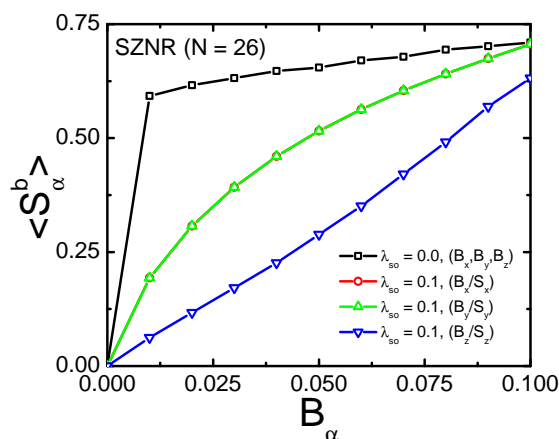


Figure 4. Band polarization $\langle S_\alpha^b \rangle$ for $\alpha = x, y, z$, as a function of magnetic field applied along the coordinate axes. The black curve is for vanishing SOC (thus the results are independent of magnetic field orientation), while the red, green, and blue curves are for magnetic field applied along the x -, y -, and z -axis, respectively, for $\lambda_{SO} = 0.1$.

In the following section, we discuss the Kondo effect when a magnetic impurity is coupled to the edge of a ZSNR (see Figure 1). To do so, we perform NRG calculations to obtain the spectral function and thermodynamic properties of this system. To this end, we use the well-known NRG Ljubljana open source code [36]. For all calculations, we have used the discretization parameter $\Lambda = 2.0$ and kept 2000 states at each iteration. We also employ the z -trick [37] (with $z = 0.2, 0.4, 0.6, 0.8$ and 1.0) to remove unwanted oscillations in the physical quantities. To map our 2×2 matrix hybridization function onto a Wilson chain we have employed the scheme proposed by Liu et al. in Ref. [33]

2.4. Results and Discussion

To obtain the following numerical results, we have considered $N = 26$, $\Gamma_{tip} = 0.01$, $U = 0.5$, and $V_0 = 0.05$ for all figures, while different sets of values for λ_{SO} and \vec{B} were used. As mentioned in the Introduction, we also considered $g_{imp} = 0$ (with $g_b = 1$) in all calculations.

In Figure 5 we show how the impurity density of states $\rho(\omega)$, at zero magnetic field (black curve in both panels), is affected by the band magnetic polarization for a magnetic field applied along \hat{x} , \hat{y} , or \hat{z} (red, green, and blue curves, respectively). Panel (a) is for vanishing SOC and panel (b) is for $\lambda_{SO} = 0.1$. In the absence of SOC and magnetic field (black curve in Figure 5a), the Kondo peak suffers a splitting at $\omega = 0$ (see black curve in the inset for a detailed view). This resembles the physical behavior discussed in Ref. [38], where the resonant level was provided by the nearby non-interacting quantum dot coupled to a metallic lead. Here, it is provided by the propagating edge state of the ribbon, as observed in the black line of Figure 2b. A similar effect has been predicted for graphene zigzag nanoribbons [31]. In addition, at the vanishing SOC, $\rho(\omega)$ is the same for all three magnetic field orientations. In the main panel, it is possible to see that the B_z result (blue curve) slightly diverges from the B_x and B_y results (red and green curves). This originates from the complexity of the Wilson chain discretization for the 2×2 matrix hybridization function that presents highly localized peaks, which somehow induce a small numerical error for a specific range of ω . For $\lambda_{SO} = 0.1$, the energy bands around $\omega = 0$ become dispersive (see Figure 2a). This strongly suppresses the very narrow peak in the DOS observed at the vanishing SOC, making it much broader, resulting in an almost flat metallic DOS at the Fermi energy. As a consequence, the Kondo peak splitting, observed for $\lambda_{SO} = 0$ in Figure 5a, caused by the very sharp peak in the DOS at the Fermi energy, is suppressed, as can be observed in more detail for the black curve (for $B = 0$) in the inset to Figure 5b. Obviously, this peak is split and suppressed once the magnetic field is switched on. In addition, for $B \neq 0$, because of SOC, $\rho(\omega)$ for B_x and B_y are identical (red and green

curves), while it differs when the field is along the z -axis. This could be already inferred from the results shown in Figure 3b–d. This reflects the fact that the SOC effective magnetic field is along the z -axis (see Appendix B). It is also interesting to notice that the splitting and suppression of the Kondo peak, for finite SOC, is stronger when the field is applied in the xy -plane than when applied along the z -direction. As shown below, this seems to occur because the band is considerably more polarized when the field is applied in the xy -plane than when it is applied along the z -direction.

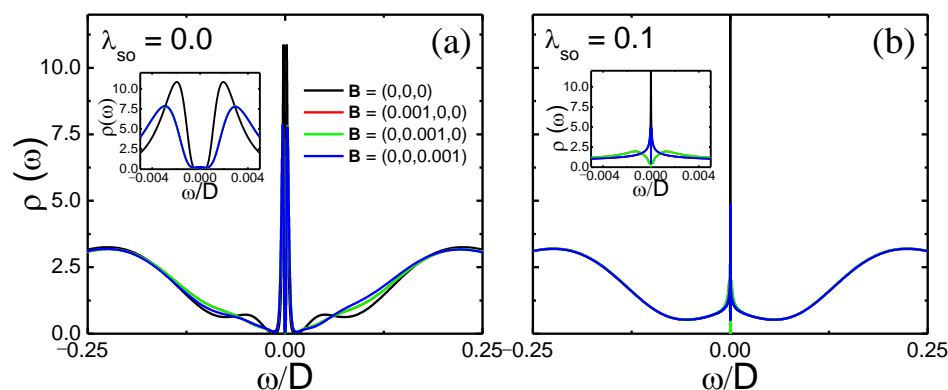


Figure 5. Impurity density of states, $\rho(\omega) = \rho_{\uparrow}(\omega) + \rho_{\downarrow}(\omega)$, for energies around the Fermi energy ($\omega = 0$). (a) Results for vanishing magnetic field (black curve) and for $|B| = 0.001$ along the three coordinate axes (see legend), with $\lambda_{SO} = 0.0$. (b) Same magnetic field values as in panel (a), but for $\lambda_{SO} = 0.1$. The insets show zooms of the Kondo peak.

To investigate how the band polarization affects the Kondo state, an analysis of the impurity polarization $\langle S_{\alpha=x,y,z}^{\text{imp}} \rangle$ dependence on the temperature and magnetic field is shown in Figure 6. We should remark that the impurity is polarized by the band; thus, at low temperatures, once the band polarization has completely destroyed the Kondo state, we should have a fully polarized impurity ($\langle S_{\alpha=x,y,z}^{\text{imp}} \rangle \sim 0.5$, at sufficiently high fields). Panel (a) shows (identical) results for $\langle S_x^{\text{imp}} \rangle$ and $\langle S_y^{\text{imp}} \rangle$, when the field is applied along the x - and y -direction, respectively, while panel (b) shows results for $\langle S_z^{\text{imp}} \rangle$ when the field is applied along the z -direction. Obviously, the other $\langle S_{\alpha}^{\text{imp}} \rangle$ components vanish. At high temperatures, as expected, all impurity magnetizations vanish for all values of field due to charge fluctuations, while, in panel (a), at low temperatures, the impurity polarization reaches a plateau, right below $\langle S_{x/y}^{\text{imp}} \rangle \lesssim 0.45$ for the highest field value. This value has increased monotonically with magnetic field from ~ 0.4 (obtained for $|B| = 10^{-4}$). A qualitatively similar picture is obtained for $\langle S_z^{\text{imp}} \rangle$ [panel (b)], with the difference that the plateaus are lower and they are formed at somewhat lower temperatures, again indicating the fact that the band polarizes more strongly for magnetic fields in the xy -plane. Thus, as observed above for the different properties, the SOC-generated anisotropy is clearly observed.

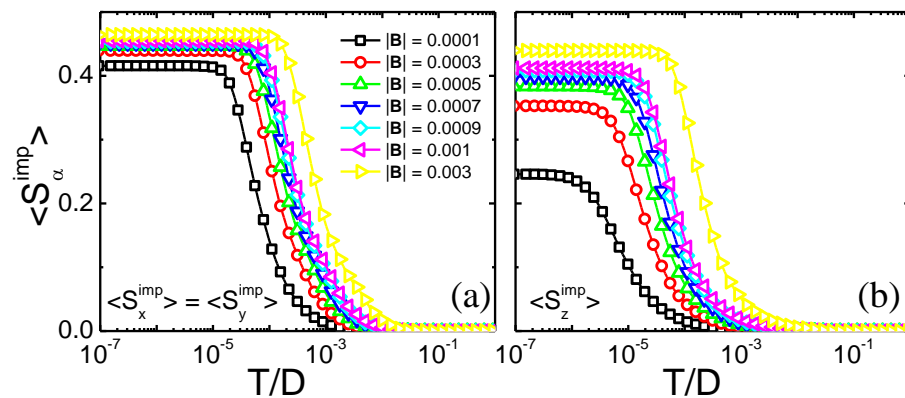


Figure 6. Impurity polarization ($\langle S_{\alpha=x,y,z}^{\text{imp}} \rangle$) as a function of temperature for different applied magnetic fields. (a) Magnetic field along x - and y -direction. (b) Same curves as in panel (a), but for magnetic field along the z -direction, with $\lambda_{\text{SO}} = 0.1$ for both panels.

3. Summary and Conclusions

In this work, we have investigated the Kondo effect in a system composed of a quantum magnetic impurity coupled to the edge of a ZSNR (in a hollow-site configuration). The ZSNR, a finite topological insulator, thus having a metallic topological edge state, is simulated by the Kane–Mele model, while the whole system is simulated by the SIAM. Our main interest is to simulate what an STM probe, analyzing the impurity, would see when the band is polarized by an external magnetic field applied along one of the coordinate axes. To emphasize the band polarization effect, we consider $g_{\text{imp}} = 0$, qualitatively similar to an experimental situation where the impurity gyromagnetic-factor is much smaller than the band gyromagnetic-factor, i.e., $g_{\text{imp}} \ll g_{\text{b}}$, something that may be experimentally achieved by a judicious choice of the impurity. It turns out that the presence of the ZSNR intrinsic SOC, responsible for an effective magnetic field applied perpendicular to the ZSNR (z -direction), results, at small magnetic fields, in a considerably smaller band polarization than when SOC vanishes. In addition, the SOC-broken SU(2) symmetry results in band polarizations that, for $|B_{\alpha} = 0.001|$, are related by $\langle S_z^b \rangle / \langle S_{x/y}^b \rangle \sim 0.2$. This considerable difference greatly magnifies the difference in what an STM sees when analyzing the impurity Kondo peak for fields along different coordinate axes. Indeed, as expected, the Kondo peak is much more strongly suppressed for a magnetic field along the x - or y -axis than along the z -axis (see inset to Figure 6b). The same anisotropy and quantitative difference are observed in the impurity polarization $\langle S_{x/y}^{\text{imp}} \rangle$ caused by the band polarization (compare panels (a) and (b) in Figure 4).

The importance of our results rests in the fact that recent advances in nanoribbon synthesis, STM sensitivity, and the STM ability to precisely place adsorbed magnetic impurities in surfaces and monolayers, allow us to propose the use of the Kondo effect, when its Kondo peak is STM-observed, to test the ability of the Kane–Mele model to describe the basic properties of ZSNRs. We hope that our results will stimulate experimental and theoretical groups alike to test our predictions.

Author Contributions: All authors contributed equally to all parts of the paper. All authors have read and agreed to the published version of the manuscript

Funding: E.V. acknowledges financial support from Conselho Nacional de Desenvolvimento Científico e Tecnológico (CNPq), processes 311366/2021-0 and 305738/2018-6, and Fundação de Amparo à Pesquisa do Estado de Minas Gerais (FAPEMIG), process PPM-00631-17. G.B.M. acknowledges financial support from the Brazilian agency Conselho Nacional de Desenvolvimento Científico e Tecnológico (CNPq), processes 424711/2018-4, 305150/2017-0 and 210 355/2018.

Institutional Review Board Statement: Not applicable.

Informed Consent Statement: Not applicable.

Data Availability Statement: Not applicable.

Conflicts of Interest: The authors declare no conflict of interest.

Abbreviations

The following abbreviations are used in this manuscript:

- GF Green’s function
- LDOS Local density of states
- NRG Numerical Renormalization Group
- SOC Spin orbit coupling
- ZNR Zigzag nanoribbon

Appendix A. Calculations for Finite g_{imp}

In an effort to soften the constraint $g_{imp} = 0$, we present, in Figure A1, results for the same parameters as in Figure 6, but now just for $|B| = 0.0001$ and four different values of $0.0 \leq g_{imp}/g_b \leq 0.3$ [see labels in panel (a)]. As can be observed from the results, a finite g_{imp}/g_b generates a monotonic increase of the plateau height for both $\langle S_x^{imp} \rangle = \langle S_y^{imp} \rangle$ and $\langle S_z^{imp} \rangle$, with the latter raising faster, but, despite that, at low temperatures there is still an anisotropy between magnetic fields in the z-direction and along the xy -plane.

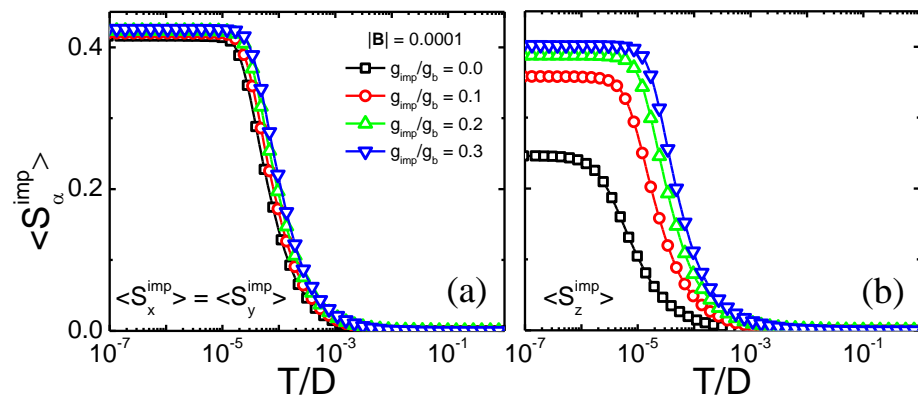


Figure A1. Same results as in Figure 6, but now just for external magnetic field strength $|B| = 0.0001$ and four different values of $0.0 \leq g_{imp}/g_b \leq 0.3$.

In case we assume that $g_b \approx 2.0$, one way of obtaining $g_{imp}/g_b < 1.0$ would be through the use of a lanthanide magnetic impurity. For example, it is well known that Pr^{3+} ions have a Landé factor of $4/5$, which, given the conservative estimate made above for g_b , results in $g_{imp}/g_b = 0.4$.

Appendix B. Hamiltonian for Bulk Silicene

The Hamiltonian for the Kane–Mele model in two-dimensions, in reciprocal space, may be written as

$$H_{KM} = \sum_{\vec{k}} \Psi_{\vec{k}}^\dagger h_{\vec{k}} \Psi_{\vec{k}}, \tag{A1}$$

where $\Psi_{\vec{k}}^\dagger = (a_{\vec{k}\uparrow}^\dagger \ b_{\vec{k}\uparrow}^\dagger \ a_{\vec{k}\downarrow}^\dagger \ b_{\vec{k}\downarrow}^\dagger)$ and

$$h_{\vec{k}} = \sigma_0 \otimes (\Delta_{\vec{k},R} \tau_x - \Delta_{\vec{k},I} \tau_y) + \Sigma_{\vec{k}} \sigma_z \otimes \tau_z - \vec{B} \cdot \vec{\sigma} \otimes \tau_0, \tag{A2}$$

where $\Delta_{\vec{k},R}$ and $\Delta_{\vec{k},I}$ are the real and imaginary parts, respectively, of the nearest-neighbor hopping term

$$\Delta_{\vec{k}} = -te^{ik_x} \left(1 + 2 \cos(\sqrt{3}k_y/2) e^{-i3k_x/2} \right), \quad (\text{A3})$$

and the k -dependent intrinsic spin-orbit term is given by

$$\Sigma_{\vec{k}} = \frac{4\lambda_{SO}}{2\sqrt{3}} \sin(\sqrt{3}k_y/2) (\sin(3k_x/2) - \cos(3k_x/2)), \quad (\text{A4})$$

where the vector of Pauli matrices $\vec{\sigma} = (\sigma_x, \sigma_y, \sigma_z)$ ($\vec{\tau} = (\tau_x, \tau_y, \tau_z)$) acts on spin (sublattice) space, with σ_0 (τ_0) the 2×2 identity matrix in spin (sublattice) space. This Hamiltonian form makes it evident that the spin-orbit term may be interpreted as a k -dependent effective magnetic field that points in the z -direction and has opposite signs for different sublattices. This explains the anisotropy of the band-polarization results shown in the main text. Indeed, based on the direction of the spin-orbit effective magnetic field, one expects that $\langle S_x^b \rangle = \langle S_y^b \rangle \neq \langle S_z^b \rangle$, as shown in Figure 4.

References and Notes

- Kane, C.L.; Mele, E.J. Quantum Spin Hall Effect in Graphene. *Phys. Rev. Lett.* **2005**, *95*, 226801. [[CrossRef](#)] [[PubMed](#)]
- Kane, C.L.; Mele, E.J. Z_2 Topological Order and the Quantum Spin Hall Effect. *Phys. Rev. Lett.* **2005**, *95*, 146802. [[CrossRef](#)] [[PubMed](#)]
- Haldane, F.D.M. Model for a Quantum Hall Effect without Landau Levels: Condensed-Matter Realization of the “Parity Anomaly”. *Phys. Rev. Lett.* **1988**, *61*, 2015. [[CrossRef](#)] [[PubMed](#)]
- König, M.; Wiedmann, S.; Brüne, C.; Roth, A.; Buhmann, H.; Molenkamp, L.W.; Qi, X.L.; Zhang, S.C. Quantum spin hall insulator state in HgTe quantum wells. *Science* **2007**, *318*, 766. [[CrossRef](#)]
- König, M.; Buhmann, H.; Molenkamp, L.W.; Hughes, T.; Liu, C.X.; Qi, X.L.; Zhang, S.C. The quantum spin Hall effect: Theory and experiment. *J. Phys. Soc. Jpn.* **2008**, *77*, 1. [[CrossRef](#)]
- Liu, C.C.; Jiang, H.; Yao, Y. Low-energy effective Hamiltonian involving spin-orbit coupling in silicene and two-dimensional germanium and tin. *Phys. Rev. B* **2011**, *84*, 195430. [[CrossRef](#)]
- Molle, A.; Goldberger, J.; Houssa, M.; Xu, Y.; Zhang, S.C.; Akinwande, D. Buckled two-dimensional Xene sheets. *Nat. Mater.* **2017**, *16*, 163. [[CrossRef](#)]
- Wei, S.; Tang, X.; Liao, X.; Ge, Y.; Jin, H.; Chen, W.; Zhang, H.; Wei, Y. Recent progress of spintronics based on emerging 2D materials: CrI(3) and Xenes. *Mater. Res. Express* **2019**, *6*, 122004. [[CrossRef](#)]
- Bhatia, I.S.; Randhawa, D.K.K. Something more than graphene - futuristic two-dimensional nanomaterials. *Curr. Sci.* **2020**, *118*, 1656. [[CrossRef](#)]
- Zhang, L.; Gong, T.; Yu, Z.; Dai, H.; Yang, Z.; Chen, G.; Li, J.; Pan, R.; Wang, H.; Guo, Z.; et al. Recent Advances in Hybridization, Doping, and Functionalization of 2D Xenes. *Adv. Funct. Mater.* **2021**, *31*, 2005471. [[CrossRef](#)]
- Balendhran, S.; Walia, S.; Nili, H.; Sriram, S.; Bhaskaran, M. Elemental Analogues of Graphene: Silicene, Germanene, Stanene, and Phosphorene. *Small* **2015**, *11*, 640. [[CrossRef](#)] [[PubMed](#)]
- Molle, A.; Grazianetti, C.; Tao, L.; Taneja, D.; Alam, M.H.; Akinwande, D. Silicene, silicene derivatives, and their device applications. *Chem. Soc. Rev.* **2018**, *47*, 6370. [[CrossRef](#)] [[PubMed](#)]
- Lyu, J.K.; Zhang, S.F.; Zhang, C.W.; Wang, P.J. Stanene: A Promising Material for New Electronic and Spintronic Applications. *Ann. Phys. (Berlin)* **2019**, *531*, 1900017. [[CrossRef](#)]
- Galbiati, M.; Motta, N.; De Crescenzi, M.; Camilli, L. Group-IV 2D materials beyond graphene on nonmetal substrates: Challenges, recent progress, and future perspectives. *Appl. Phys. Rev.* **2019**, *6*, 041310. [[CrossRef](#)]
- Hartman, T.; Sofer, Z. Beyond Graphene: Chemistry of Group 14 Graphene Analogues: Silicene, Germanene, and Stanene. *ACS Nano* **2019**, *13*, 8566. [[CrossRef](#)] [[PubMed](#)]
- Ezawa, M. A topological insulator and helical zero mode in silicene under an inhomogeneous electric field. *New J. Phys.* **2012**, *14*, 033003. [[CrossRef](#)]
- Ezawa, M. Monolayer Topological Insulators: Silicene, Germanene, and Stanene. *J. Phys. Soc. Jpn.* **2015**, *84*, 121003. [[CrossRef](#)]
- Yaroshevich, A.S.; Kvon, Z.D.; Gusev, G.M.; Mikhailov, N.N. Microwave Photoresistance of a Two-Dimensional Topological Insulator in a HgTe Quantum Well. *J. Exp. Theor. Phys. Lett.* **2020**, *111*, 121. [[CrossRef](#)]
- Kvon, Z.D.; Kozlov, D.A.; Olshanetsky, E.B.; Gusev, G.M.; Mikhailov, N.N.; Dvoretzky, S.A. Topological insulators based on HgTe. *Physics-Uspokhi* **2020**, *63*, 629. [[CrossRef](#)]
- König, M. Spin-Related Transport Phenomena in HgTe-Based Quantum Well Structures. Ph.D. Thesis, Universität Würzburg, Würzburg, Germany, 2007.
- Anderson, P.W. Localized Magnetic States in Metals. *Phys. Rev.* **1961**, *124*, 41. [[CrossRef](#)]

22. Hewson, A.C. *The Kondo Problem to Heavy Fermions*; Cambridge University Press: Cambridge, UK, 1993. [[CrossRef](#)]
23. Hsu, C.H.; Stano, P.; Klinovaja, J.; Loss, D. Helical liquids in semiconductors. *Semicond. Sci. Technol.* **2021**, *36*, 123003. [[CrossRef](#)]
24. Goth, F.; Luitz, D.J.; Assaad, F.F. Magnetic impurities in the Kane-Mele model. *Phys. Rev. B* **2013**, *88*, 075110. [[CrossRef](#)]
25. Allerdt, A.; Feiguin, A.E.; Martins, G.B. Spatial structure of correlations around a quantum impurity at the edge of a two-dimensional topological insulator. *Phys. Rev. B* **2017**, *96*, 035109. [[CrossRef](#)]
26. Allerdt, A.; Feiguin, A.; Martins, G. Kondo effect in a two-dimensional topological insulator: Exact results for adatom impurities. *J. Phys. Chem. Solids* **2019**, *128*, 202. [[CrossRef](#)]
27. Büsser, C.A.; Martins, G.B.; Feiguin, A.E. Lanczos transformation for quantum impurity problems in d -dimensional lattices: Application to graphene nanoribbons. *Phys. Rev. B* **2013**, *88*, 245113. [[CrossRef](#)]
28. Allerdt, A.; Büsser, C.A.; Martins, G.B.; Feiguin, A.E. Kondo versus indirect exchange: Role of lattice and actual range of RKKY interactions in real materials. *Phys. Rev. B* **2015**, *91*, 085101. [[CrossRef](#)]
29. Weymann, I.; Zwierzycki, M.; Krompiewski, S. Spectral properties and the Kondo effect of cobalt adatoms on silicene. *Phys. Rev. B* **2017**, *96*, 115452. [[CrossRef](#)]
30. Vernek, E.; Martins, G.B.; Žitko, R. Anisotropic Kondo screening induced by spin-orbit coupling in quantum wires. *Phys. Rev. B* **2020**, *102*, 155114. [[CrossRef](#)]
31. Diniz, G.S.; Luiz, G.I.; Latgé, A.; Vernek, E. From Kondo to local singlet state in graphene nanoribbons with magnetic impurities. *Phys. Rev. B* **2018**, *97*, 115444. [[CrossRef](#)]
32. Nakada, K.; Fujita, M.; Dresselhaus, G.; Dresselhaus, M.S. Edge state in graphene ribbons: Nanometer size effect and edge shape dependence. *Phys. Rev. B* **1996**, *54*, 17954. [[CrossRef](#)]
33. Liu, J.G.; Wang, D.; Wang, Q.H. Quantum impurities in channel mixing baths. *Phys. Rev. B* **2016**, *93*, 035102. [[CrossRef](#)]
34. Osolin, V.; Žitko, R. Fine structure of the spectra of the Kondo lattice model: Two-site cellular dynamical mean-field theory study. *Phys. Rev. B* **2017**, *95*, 035107. [[CrossRef](#)]
35. Demchenko, D.O.; Joura, A.V.; Freericks, J.K. Effect of Particle-Hole Asymmetry on the Mott-Hubbard Metal-Insulator Transition. *Phys. Rev. Lett.* **2004**, *92*, 216401. [[CrossRef](#)] [[PubMed](#)]
36. Žitko, R. NRG Ljubljana. 2021. Available online: <https://zenodo.org/record/4841076#.Y11EmOFByUk> (accessed on 8 May 2021).
37. Campo, V.L.; Oliveira, L.N. Alternative discretization in the numerical renormalization-group method. *Phys. Rev. B* **2005**, *72*, 104432. [[CrossRef](#)]
38. Dias da Silva, L.G.G.V.; Sandler, N.P.; Ingersent, K.; Ulloa, S.E. Zero-Field Kondo Splitting and Quantum-Critical Transition in Double Quantum Dots. *Phys. Rev. Lett.* **2006**, *97*, 096603. [[CrossRef](#)]